



Interstitial boron-doped Ni₄Mo nanoarray catalyst boosts stable hydrogen evolution reaction

Pengfei Liu^a, Yue Shi^a, Xin Zhang^a, Jiao Yin^a, Dan Zhang^c, Tiantian Wang^a, Jiawei Fei^a, Tianrong Zhan^a, Guangjiu Li^a, Jianping Lai^{a,*}, Lei Wang^{a,b,**}

^a State Key Laboratory Base of Eco-Chemical Engineering, Ministry of Education, International Science and Technology Cooperation Base of Eco-chemical Engineering and Green Manufacturing, College of Chemistry and Molecular Engineering, Qingdao University of Science and Technology, Qingdao 266042, PR China

^b Shandong Engineering Research Centre for Marine Environment Corrosion and Safety Protection, College of Environment and Safety Engineering, Qingdao University of Science and Technology, Qingdao 266042, PR China

^c Key Laboratory of Catalytic Conversion and Clean Energy in Universities of Shandong Province, School of Chemistry and Chemical Engineering, Qufu Normal University, Qufu, Shandong 273165, PR China

ARTICLE INFO

Keywords:

Interstitial doping
Ni₄Mo nanorod arrays
Mo dissolution
Anion-exchange membrane
Hydrogen evolution reaction

ABSTRACT

Designing a strategy to make the intrinsic activity of NiMo-based catalysts while being able to achieve long-term stable hydrogen production at ampere-level current densities is important for their development in AEM electrolyzers. Herein, interstitial boron atom-doped Ni₄Mo is designed to obtain the catalyst with excellent alkaline HER properties. B₄₋₇-Ni₄Mo/NF exhibits a small overpotential of 135.2 mV at 1000 mA cm⁻² and a high turnover frequency (TOF) value of 6.14 s⁻¹ at 100 mV in alkaline HER, which very close to that of Pt/C (6.86 s⁻¹). The catalyst requires only 1.73 V to achieve a current density of 1.0 A cm⁻² in AEM electrolyzer at 60 °C and is stable for 800 h. Experimental and theoretical calculations reveal that interstitial boron doping not only optimizes the electronic structure to optimize H^{*} adsorption and promote the water dissociation but also inhibits the dissolution of Mo by forming boron-metal bond.

1. Introduction

The development of low-carbon clean hydrogen energy has become a global consensus.[1,2] The electrolytic water hydrogen production technology is a breakthrough in the supply of low-carbon clean hydrogen (H₂) fuels, which will become an important area to support the development of new energy with high proportion and the construction of hydrogen power synergy pattern in the future.[3,4] Electrolysis of water using solid polymer-based anion exchange membranes (AEM) is the preferred technology for future large-scale hydrogen production.[5] Compared to proton exchange membrane (PEM) water electrolysis,[6] AEM has lower ohmic resistance, less mass transfer loss, and lower manufacturing costs.[7] The crucial aspect in advancing AEM electrolytic water hydrogen production technology is to identify catalysts with high intrinsic activity and exceptional durability for reliable hydrogen production at ampere-level current densities.[8,9] Currently, Pt[10] has the most excellent intrinsic activity and stability and is the most

commonly used HER catalyst in AEM electrolyzer.[11] However, the expensive price and scarcity of Pt limit the large-scale commercialization of AEM electrolysis water.[7] Therefore, the development of non-precious metal catalysts capable of high activity and long-term stability at high current densities has become a hot research topic. Among the non-precious metals, NiMo-based catalysts with nanorod array structure[12] are very promising in alkaline HER. This is mainly attributed to the excellent charge transfer ability, low mass transfer resistance and high gas release rate of the nanorod array structure[13], and the excellent water dissociation ability of Ni and the good adsorption of Mo to H^{*}. [14] Up to now, the electronic structure has been mainly adjusted by construction of heterogeneous interfaces,[12,15] synthesis of metal compounds,[16,17] metal doping,[9] and adjustment of Ni and Mo ratios[18] to optimize the adsorption of H^{*} or accelerate water dissociation, thus improving the intrinsic activity of NiMo-based catalysts. However, it remains a challenge to optimize H^{*} adsorption while improve the water dissociation ability of NiMo-based catalysts.

* Corresponding author.

** Corresponding author at: Shandong Engineering Research Centre for Marine Environment Corrosion and Safety Protection, College of Environment and Safety Engineering, Qingdao University of Science and Technology, Qingdao 266042, PR China

E-mail addresses: jplai@qust.edu.cn (J. Lai), inorchemwl@126.com (L. Wang).

<https://doi.org/10.1016/j.apcatb.2023.123332>

Received 11 August 2023; Received in revised form 13 September 2023; Accepted 22 September 2023

Available online 23 September 2023

0926-3373/© 2023 Elsevier B.V. All rights reserved.

More importantly, it has been found that in alkaline HER, Mo is easily dissolved [14,19] by alkaline solution corrosion, resulting in the decline of catalyst stability. Researchers have used chemically stable materials, such as graphene [20], C_3N_4 [21] or Cr [22], to coat NiMo-based catalysts to prevent Mo dissolution. However, these approaches clog the active site. Some researchers have also inhibited the dissolution of Mo by changing different alkaline cationic electrolytes and reducing pH [23], but these measures inevitably reduce catalytic activity. Therefore, designing a strategy to make the intrinsic activity of NiMo-based catalysts comparable to that of Pt/C while being able to achieve long-term stable hydrogen production at ampere-level current densities is important for their development in AEM electrolyzers.

Here, we design an interstitial boron atom doping strategy and report that a new class of interstitial boron (B) atoms doped Ni_4Mo nanoarrays (B_x-Ni_4Mo/NF , X = the atomic percentage of B doping, NF= nickel foam) synthesized on nickel foam. Density functional theory (DFT) calculation confirms that electron-deficient B doping can modulate the electronic structure of Ni_4Mo , optimize the adsorption strength of H^* and promote the dissociation of water. Electron interactions between Mo and B stabilize the Mo atom. The formation of boron-metal bond can effectively weaken the adsorption of OH^- by reducing the oxytropy of Mo, thus inhibiting the dissolution of Mo in alkaline HER. The results show $B_{4.7}-Ni_4Mo/NF$ exhibits excellent catalytic in alkaline HER with a small overpotential of 135.2 mV at 1000 mA cm^{-2} , a low Tafel slope of 37.2 mV dec^{-1} and a turnover frequency (TOF) value of 6.14 s^{-1} at 100 mV in alkaline media. Moreover, the $B_{4.7}-Ni_4Mo/NF$ requires only 1.73 V to reach a current density of 1.0 A cm^{-2} in a 60 °C electrolyzer and can operate stably at that current density for 800 h. It is one of the non-precious metals electrocatalysts with the best comprehensive performance in AEM electrolyzer so far.

2. Methods and experimental section

2.1. Chemicals

Nickel (II) nitrate hexahydrate ($Ni(NO_3)_2 \cdot 6 H_2O$, $\geq 98\%$) was from Alfa Aesar. Ammonium molybdate tetrahydrate ($(NH_4)_6Mo_7O_{24} \cdot 4 H_2O$) was purchased from China National Medicines Corporation Ltd. Boric acid (H_3BO_3 , 99%) was purchased from Aladdin.

2.2. Synthesis of $NiMoO_4$ nanorod arrays on NF

First, the NF was cut into a rectangular shape with an area of 1.0 $cm \times 2.0$ cm. Second, the pieces of NF were washed with 3 M HCl, ethanol and deionized water, respectively. Thirdly, 4 mmol of $Ni(NO_3)_2 \cdot 6 H_2O$, 0.14 mmol of $(NH_4)_6Mo_7O_{24} \cdot 4 H_2O$ (Ni: Mo=4:1), and 15 mL of deionized water were combined in a 25 mL Teflon autoclave and thoroughly dissolved. Lastly, the autoclave was sealed and subjected to 150 °C for 6 h. Upon natural cooling, the NF bearing the products was retrieved, rinsed with deionized water, and air-dried. We obtained $NiMoO_4$ nanorod arrays.

2.3. Synthesis of Ni_4Mo/NF alloy on NF

$NiMoO_4$ nanorod arrays obtained by the above method were heated at 500 °C for 3 h in a H_2/Ar (20:80) atmosphere in a tubular furnace and got Ni_4Mo/NF . The loading mass of Ni_4Mo on nickel foam was 3.61 mg cm^{-2} .

2.4. Synthesis of $B_{4.7}-Ni_4Mo/NF$ nanorod arrays on NF

100 mg H_3BO_3 was dissolved in 1 mL of deionized water and completely dissolved by ultrasound. Subsequently, the prepared dispersion (100 μL) was slowly dropped onto $NiMoO_4/NF$ covering an area of 1.0 $cm \times 2.0$ cm and dried in air. Then, it was heated at 500 °C for 3 h in a H_2/Ar (20:80) atmosphere in a tubular furnace and got $B_{4.7}-$

Ni_4Mo/NF . The loading mass of $B_{4.7}-Ni_4Mo$ on nickel foam was 3.97 mg cm^{-2} .

2.5. Synthesis of Pt/C catalyst on NF

A mixture of 20 mg Pt/C, 30 μL Nafion, 270 μL ethanol, and 200 μL deionized water was sonicated for 20 min. Subsequently, the prepared dispersion (100 μL) was slowly dropped onto nickel foam covering an area of 1.0 $cm \times 1.0$ cm and dried in air. the loading mass of Pt/C on nickel foam was about 4 mg cm^{-2} .

2.6. Synthesis of IrO_2 catalyst on NF

The synthesis method is similar to the above, except that commercial Pt/C is replaced by IrO_2 .

2.7. Characterization

The morphology and structure of the catalyst was preliminarily studied by using a Hitachi S-4800 SEM scanning. The structure of catalyst was further characterized by FEI Tecnai-G2 F30 transmission electron microscope (TEM) and high-resolution TEM (HRTEM) tests at an accelerating voltage of 300 kV. X'Pert-PRO MPD diffractometer was used to obtain powder X-ray diffraction (XRD) images under 40 kV and 40 mA Cu K α radiation, and then the results were compared with MDI jade. The Axis Supra spectrometer was carried for X-ray photoelectron spectroscopy (XPS) analysis by using a monochromatic Al K α source (15 mA, 14 kV). The processed data was determined for the catalyst's valence state using Casa XPS software. The content of H_2 was analyzed by gas chromatography (GC-7890B, Agilent, America, TCD, MS-5 A molecular sieve column, Ar as carrier gas). The catalyst and solution elements were determined by inductively coupled plasma atomic emission spectrometer (ICP-AES, V arian 710-ES). The catalyst was further characterized after stability test.

2.8. Electrochemical measurements

The electrochemical measurements were conducted with a Gamry Reference 3000 electrochemical workstation, with a graphite rod utilized as the counter electrode and a saturated calomel electrode (SCE) as the reference electrode. The working electrode was comprised of the catalyst supported on nickel foam that was prepared beforehand. The relevant potential in this experiment was calculated using the following formula for the reversible hydrogen electrode (RHE): $E(RHE) = E(Hg/HgO) + 0.098 V + 0.059 pH$. All potentials reported in this work are corrected using reversible hydrogen electrodes (RHE) and all electrochemical curves were collected by the workstation and underwent 95% iR compensation. The catalysts' performance for HER was assessed via LSV at a scan rate of 1 mV s^{-1} in a 1.0 M KOH solution, and EIS measurements were taken at a frequency of 0.1 Hz to 100 kHz in the same solution. To measure the electrochemically active surface area, cyclic voltammetry (CV) was performed at different scan rates (20–100 mV s^{-1}). The durability test was performed in 1.0 M KOH solution using chronoamperometry. Furthermore, the catalyst's stability was evaluated by measuring the LSV after 10,000 cycles of CV.

2.9. In-situ Fourier transform infrared spectroscopy (FTIR) technique

Operation process of silicon plane gold plating film: preparation of gold plating solution. Solution A was prepared: 0.1222 g NaOH and 0.2286 g $NaAuCl_4 \cdot 2 H_2O$ were dissolved in 3 mL deionized water and ultrasonic for 1 h. Solution B: 0.134 g NH_4Cl , 0.9468 g Na_2SO_3 , 0.6202 g $Na_2S_2O_3 \cdot 5 H_2O$ were dissolved in 50 mL deionized water and dispersed by ultrasound for 1 h. A solution was mixed with B solution, 50 mL of deionized water was added, and full ultrasound was performed for 2 h. Silicon crystal electroplating preparation: Firstly, soaked the silicon

crystal in Aqua regia ($V_{\text{HCl}}: V_{\text{HNO}_3} = 3:1$) for 30 min, and then washed with deionized water. Secondly, the 50 μm Al_2O_3 powder is used to grind the silicon plated crystal on the electrode cloth clockwise for 10 min, and then clean it with deionized water. Thirdly, deionized water and acetone were alternately treated 5 times, respectively for 2 min, 1 min, 1 min, 1 min, 2 min. Fourth, use an oxidizing solution ($V_{\text{H}_2\text{SO}_4}: V_{\text{H}_2\text{O}_2} = 3:1$), remove and rinse with deionized water. Finally, the silicon wafers are soaked in 40% NH_4F solution for 4–5 min and washed with deionized water. Gold film deposition: First, 15 mL gold plating solution was put into a 25 mL beaker, preheated in a 50–55 $^\circ\text{C}$ water bath for 2 min, and 3.4 mL 2% HF solution was added. Then the prepared silicon crystals are soaked in the above solution for 4–5 min, and finally washed with deionized water to obtain a gold-plated layer.

2.10. In situ Raman technique

Raman spectra were acquired with a Renishaw inVia reflection Raman microscope utilizing a 532 nm laser excitation, while controlling the potential with an electrochemical workstation. The reference electrode utilized was an Hg/HgO electrode, with an inner electrolyte of 1.0 M KOH .

2.11. Measurement of electrochemical active surface area (ECSA)

To estimate the ECSA values of materials, the double-layer capacitance (C_{dl}) was measured using a cyclic voltammetry method. The chosen potential window was outside the possible faradic region of the material and CVs were recorded at scan rates ranging from 20 to 100 mV s^{-1} . The capacitive current density, $\Delta J/2$, was linearly related to scan rate and C_{dl} was calculated from the slopes of these straight lines. C_{dl} was further converted into ECSA using the specific capacitance value (~ 0.04 mF) of a standard 1.0 cm^{-2} surface.

$$\text{ECSA} = \frac{C_{\text{dl}}}{C_s}$$

$$C_s = 0.04 \text{ mF cm}^{-2}$$

2.12. Turnover frequency calculation (TOF)

We selected an electrochemical method to obtain the TOF values of each sample. All the surface-active sites were assumed to be accessible by the electrolyte, then the TOF value could be calculated by the following equation:

$$\text{TOF} = \frac{I}{2 * n * F}$$

where I , n , and F are the current during linear sweep measurement, the number of active site number, and the Faraday constant, respectively. The factor 1/2 is because water electrolysis requires two electrons to evolve one hydrogen molecule from two protons. The number of active sites (n) is determined by integrating the CV within the potential range of -0.2 V to $+0.6$ V versus RHE in 1 M phosphate buffer solution ($\text{pH}=7$). We can evaluate the upper limit of the active site number according to the follow formula:

$$n = \frac{Q_{\text{cv}}}{2 * F}$$

where the Q represent the whole charge of CV curve.

2.13. The assembly and performance test of MEAs

The synthesized $\text{B}_{4.7}\text{-Ni}_4\text{Mo}/\text{NF}$ was used as the cathode layer and IrO_2/NF as the anode layer. An anion exchange membrane (Sustainion

X37–50) is then sandwiched between the positive and negative electrodes and a membrane electrode assembly (MEA) device is made. The flow of 1 M KOH solution is used as the electrolyte, and the temperature of the electrolyte is controlled at 60 $^\circ\text{C}$ by constant temperature heating chamber. The scan rate is 1 mV s^{-1} .

2.14. Calculation setup

All DFT calculations were conducted using the Vienna ab initio simulation package (VASP), employing plane-wave basis sets and the projector augmented-wave approach. The pathway of hydrogen evolution reaction (HER) were calculated as: $* \rightarrow * \text{H} \rightarrow * + \text{H}_2$ (Volmer-Heyrovsky). The NiMo slab model consisted of 4 at. layers of Ni and Mo ; the NiMo-B slab model consisted of 4 at. layers of Ni and Mo ; 2 atoms of B were doped into gap of layers. A 16 \AA lattice constant along the z -axis was set to avoid the layer image coupling caused by the periodic model. The exchange-correlation potential was calculated using a generalized gradient approximation (GGA) with the Perdew-Burke-Ernzerhof (PBE) parametrization. To avoid slab-slab interaction, a vacuum region of 16 \AA was employed. The surface structure was optimized using an energy cutoff of 450 eV and a dense $3 \times 3 \times 1$ k-point mesh. For DOS simulation, a dense $19 \times 19 \times 1$ k-point mesh was utilized. The atomic positions were fully relaxed until the maximum force on each atom was less than 0.02 eV/ \AA , with an energy convergence standard of 10^{-5} eV. The Gibbs free energy change (ΔG) for each elemental step is defined as:

$$\Delta G = \Delta E + \Delta \text{ZPE} - T\Delta S + \Delta G_U + \Delta G_{\text{pH}}$$

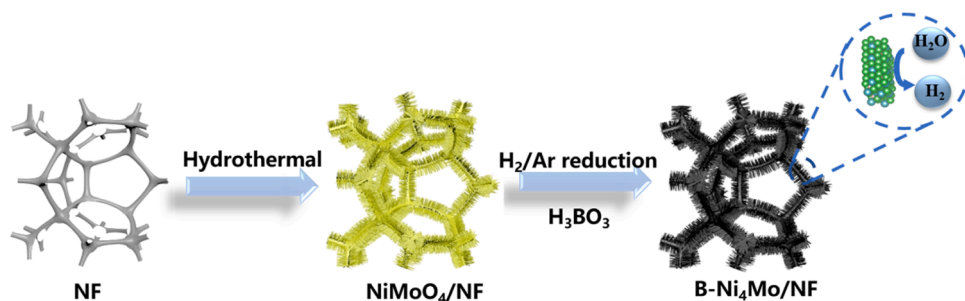
where ΔE and ΔZPE are the adsorption energy based on density functional theory calculations and the zero-point energy correction, respectively. T , ΔS , U , and ΔG_{pH} represent the temperature, the entropy change, the applied electrode potential, and the free energy correction of the pH, respectively. calculations. The enthalpy of Mo within bulk hexagonal close-packed Mo and H within H_2 were used to compute the chemical potential of Mo and H .

3. Results and discussions

3.1. Synthesis and characterizations

A two-step method was utilized to dope interstitial Boron atoms into the Ni_4Mo lattice (Scheme 1). Initially, NiMoO_4 was hydrothermally synthesized on NF. Thereafter, a boric acid mixture was dropwise added, dried and transferred to a tube furnace for thermal reduction under H_2/Ar atmosphere. Consequent to the reduction of boric acid, Boron atoms diffused in situ into the Ni_4Mo bimetallic lattice to obtain the interstitial B-doped $\text{Ni}_4\text{Mo}/\text{NF}$ ($\text{B}_x\text{-Ni}_4\text{Mo}/\text{NF}$). Prior to the hydrothermal reaction, the NF was treated with 3 M HCl solution via sonication for several minutes to enhance its roughness and facilitate loading, as revealed in the SEM image depicted in Fig. S1. The morphology of the NiMoO_4/NF was observed by SEM, which revealed dense and smooth arrays of $\text{NiMoO}_4 \cdot x\text{H}_2\text{O}$ nanorods arranged vertically on nickel foam (Figs. S2a and 2b).

The $\text{B}_x\text{-Ni}_4\text{Mo}$ powder sonicated off of nickel foam was quantified by using inductively coupled plasma-atomic emission spectrometry (ICP-AES) and the results are presented in Table S1. The morphology of $\text{B}_{4.7}\text{-Ni}_4\text{Mo}/\text{NF}$ was examined through scanning electron microscopy (SEM) and transmission electron microscopy (TEM) for further characterization. We can observe that it maintained the same nanorod array structure as NiMoO_4/NF . The nanorod array grows neatly on the NF (Fig. 1a), providing a rich channel for gas release. The nanorods exhibit a cuboid shape and possess a rough surface (Fig. 1b-c). Furthermore, they contain numerous minute pores within their structure (Fig. 1d). This rough and porous configuration facilitates the exposure of more active sites and enhances the rapid diffusion of gases. We also synthesized $\text{Ni}_4\text{Mo}/\text{NF}$ by direct H_2/Ar reduction of NiMoO_4/NF and observed that it maintains the



Scheme 1. Synthesis process for B_x-Ni₄Mo on NF. HE. g. 1 Characterization of Pt61Ga39 @CNT. (a) SEM image. (b) TEM image (HR-TEM insert). (c) Corresponding TEM mapping. (d) Corresponding TEM line-scanning. (e) XRD pattern.

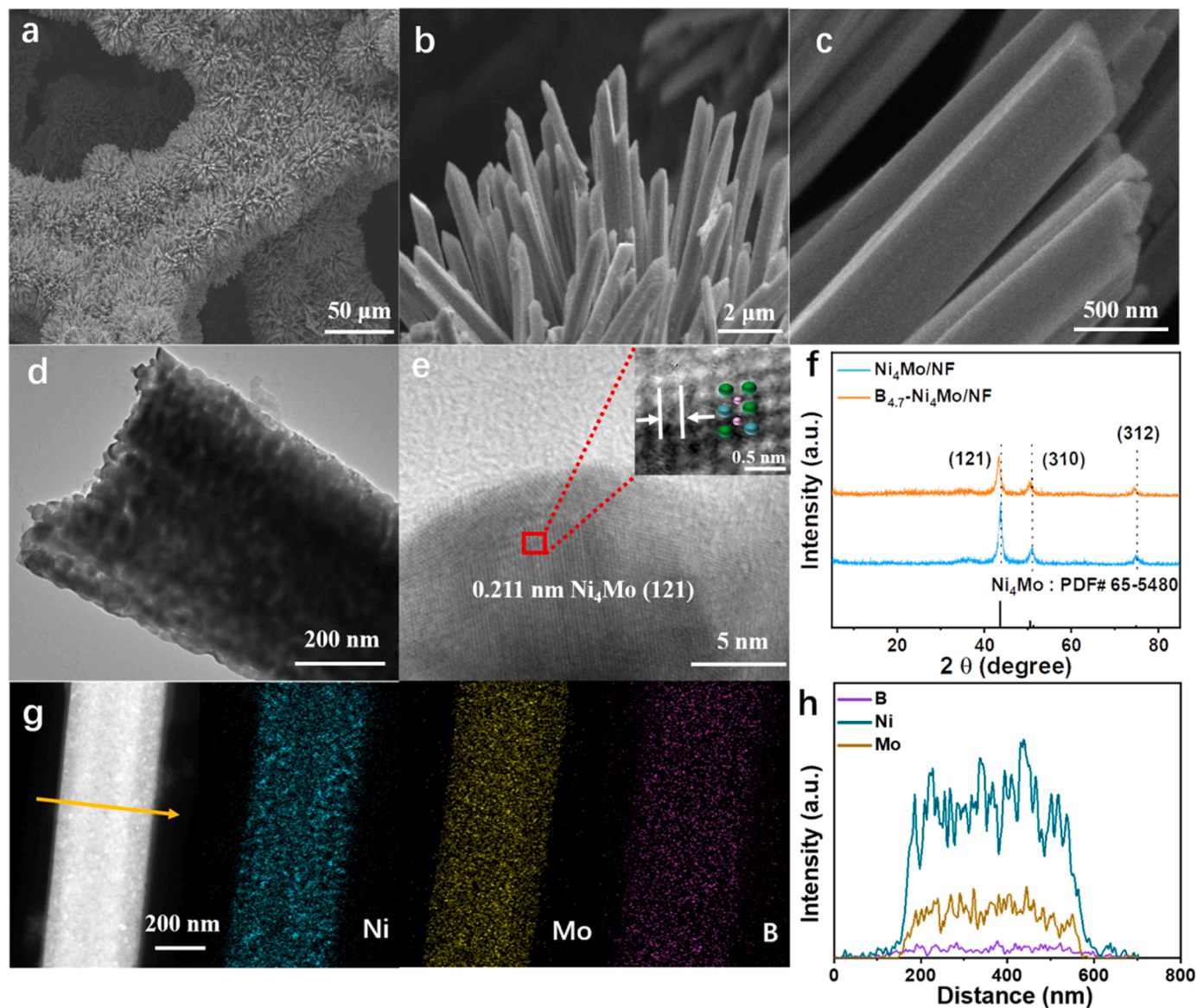


Fig. 1. (a-c) SEM images of B_{4.7}-Ni₄Mo/NF. (d) TEM image of B_{4.7}-Ni₄Mo/NF. (e) HRTEM image and FFT pattern (conversion of yellow box) of B_{4.7}-Ni₄Mo/NF; Light green, blue, pink spheres representing Ni, Mo, B atoms. (f) XRD patterns of Ni₄Mo/NF and B_{4.7}-Ni₄Mo/NF. (g) STEM image and corresponding EDS mapping image of B_{4.7}-Ni₄Mo/NF. (h) EDS line scans of B_{4.7}-Ni₄Mo/NF.

same structure as B_{4.7}-Ni₄Mo/NF (Fig. S3). Subsequently, we analyzed the XRD patterns of Ni₄Mo and B_{4.7}-Ni₄Mo powders to investigate their crystal structure. In order to characterize Ni₄Mo and B-Ni₄Mo more precisely, we sonicated them off the nickel foam for characterization. As

illustrated in Fig. 1 f, the peaks observed at 43.5°, 50.4°, and 74.7° correspond to the (121), (310), and (312) crystal planes of Ni₄Mo (PDF #65-5480). These results confirm the successful synthesis of Ni₄Mo. Compared to Ni₄Mo, B_{4.7}-Ni₄Mo exhibits a significantly reduced peak

size accompanied by a minor shift down to 20. This suggests that the interstitial sites of B are occupied, leading to the enlargement of the Ni_4Mo metal lattice at room temperature.[24,25] The high-resolution transmission electron microscopy (HRTEM) and fast Fourier transform (FFT) of the HRTEM pattern (Fig. 1e) exhibit apparent lattice fringes with a spacing of 0.211 nm, corresponding to the (121) plane of Ni_4Mo . The lattice spacing of $\text{B}_{4.7}\text{-Ni}_4\text{Mo}$ is expanded by approximately 0.04 nm in comparison to that of Ni_4Mo (0.207 nm in Fig S3d), indicating the incorporation of interstitial B atoms within the lattice. [26–28] To confirm the successful integration of interstitial boron atoms into Ni_4Mo , STEM and EDS elemental analyses were conducted to provide information on composition and the distribution of elements (Fig. 1 g). The distribution of Ni, Mo, and B was found to be uniform throughout the nanorod. Furthermore, EDS line scanning (Fig. 1 h) clearly showed that B was primarily associated with the Ni and Mo elements, suggesting that B was absorbed by Ni_4Mo . SEM images (Fig. S4) and XRD patterns (Fig. S5) were used to characterize $\text{B}_x\text{-Ni}_4\text{Mo/NF}$ samples with varying levels of B doping. While the catalysts' morphology remained unchanged, the intensity of the peaks weakened as the B doping level increased, indicating that introducing interstitial B had an impact on the crystallinity of Ni_4Mo .

Prior studies have shown that molybdenum exhibits strong oxytropy and can quickly oxidize to Mo^{4+} , which is subsequently transformed into the more reliable Mo^{6+} . [14,18,23] This result can be further demonstrated through XPS analysis. We conducted an evaluation of the XPS spectra for $\text{Ni}_4\text{Mo/NF}$ and $\text{B}_{4.7}\text{-Ni}_4\text{Mo/NF}$ (Fig. 2a–c). The valence states of Mo in $\text{Ni}_4\text{Mo/NF}$ and $\text{B}_{4.7}\text{-Ni}_4\text{Mo/NF}$ differ (Fig. 2a). In $\text{Ni}_4\text{Mo/NF}$, we observed three sets of peaks. Specifically, the peaks at 227.6 eV and 231.0 eV are attributed to Mo^0 3d_{5/2} and 3d_{3/2}, respectively. Meanwhile, Mo^{4+} 3d peaks were identified at 228.5 eV and 232.0 eV for 3d_{5/2} and 3d_{3/2}, respectively. Lastly, we noted that the peaks at 232.2 eV and 235.4 eV were attributed to Mo^{6+} 3d_{5/2} and 3d_{3/2}, respectively.[19,29] The presence of both Mo^{4+} and Mo^{6+} on the Ni_4Mo surface indicates partial oxidation of Mo. However, in the case of interstitial B-doped $\text{Ni}_4\text{Mo/NF}$, the Mo^{4+} peak reduces significantly, and Mo^{6+} peak is absent. This suggests that interstitial B atoms weaken Mo's

oxytropy and prevent oxidation. It is worth noting that, in comparison with $\text{Ni}_4\text{Mo/NF}$, $\text{B}_{4.7}\text{-Ni}_4\text{Mo/NF}$ shows a 0.4 eV positive shift in the peak towards higher binding energy direction for Mo^0 . Meanwhile, the peak for Mo^{4+} also shifts accordingly, proving the strong interaction between Mo and B. [30–33] This indicates that the interstitial B atoms regulate the electronic structure of $\text{Ni}_4\text{Mo/NF}$ [34,35]. The XPS spectra of Ni 2p (Fig. 2b) indicate that the binding energy of Ni in $\text{B}_{4.7}\text{-Ni}_4\text{Mo/NF}$ is slightly positively shifted (0.3 eV) compared to $\text{Ni}_4\text{Mo/NF}$, indicating that the electronic structure of $\text{Ni}_4\text{Mo/NF}$ is impacted by the presence of B atoms. [36]. However, the B atoms doping have significantly less effect on Ni than on Mo, probably because the Ni content is larger than Mo and the B atom can only partially affect the Ni atoms. The B 1s XPS spectrum of $\text{B}_{4.7}\text{-Ni}_4\text{Mo/NF}$ (Fig. 2c) shows a peak at 188.4 eV belonging to the boron and metal bonding. [32,37,38] Furthermore, a small peak observed at 192.5 eV can be attributed to the B–O bond, which is due to the inevitable oxidation of the interstitial B atoms exposed to oxygen on the surface. [37] Furthermore, an XPS spectrum of $\text{NiMoO}_4\text{/NF}$ was also acquired (Fig. S6). The results suggest that interstitial-B doping induces the redistribution of Ni_4Mo electrons and attracts them to fill the vacant orbital of the electron-deficient B atom, while also forming boron-metal bond. This not only regulates the electronic structure of $\text{Ni}_4\text{Mo/NF}$, but also attenuates the oxytropy of Mo and subsequently decreases the adsorption of oxygen-containing ions such as OH^- .

3.2. Electrocatalytic HER performance

We investigated the electrocatalytic properties of $\text{B}_x\text{-Ni}_4\text{Mo/NF}$ in a three-electrode system with 1.0 M KOH. By optimizing the amount of B doping, $\text{B}_{4.7}\text{-Ni}_4\text{Mo/NF}$ showed the best catalytic performance (Fig. S7). Firstly, we compared the HER performance of $\text{B}_{4.7}\text{-Ni}_4\text{Mo/NF}$ with $\text{Ni}_4\text{Mo/NF}$, $\text{NiMoO}_4\text{/NF}$, and Pt/C under the same test conditions. The linear scanning voltammetry (LSV) curves show that $\text{B}_{4.7}\text{-Ni}_4\text{Mo/NF}$ has superior HER performance (Fig. 3a). The overpotential of $\text{B}_{4.7}\text{-Ni}_4\text{Mo/NF}$ at 100 mA cm^{−2} current density is only 47.44 mV, which is better than that of $\text{Ni}_4\text{Mo/NF}$ (60.24 mV) and Pt/C (62.80 mV), indicating that the introduction of interstitial B atoms improves the HER performance of

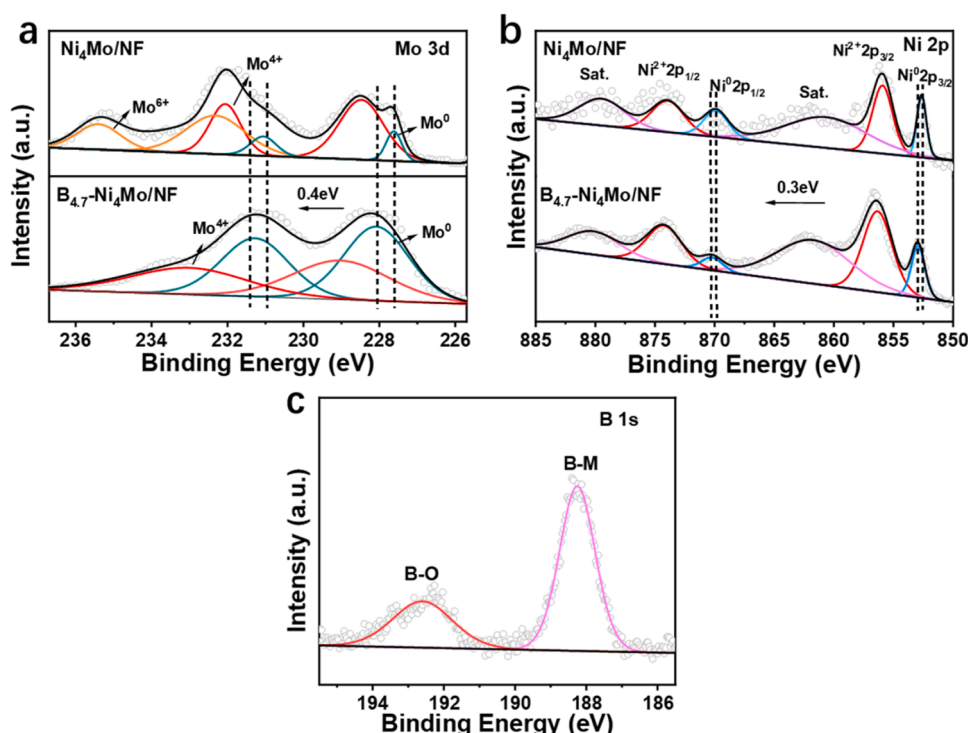


Fig. 2. XPS spectra of (a) Mo 3d, (b) Ni 2p for $\text{Ni}_4\text{Mo/NF}$ and $\text{B}_{4.7}\text{-Ni}_4\text{Mo/NF}$. (c) XPS spectrum of B 1s for $\text{B}_{4.7}\text{-Ni}_4\text{Mo/NF}$.

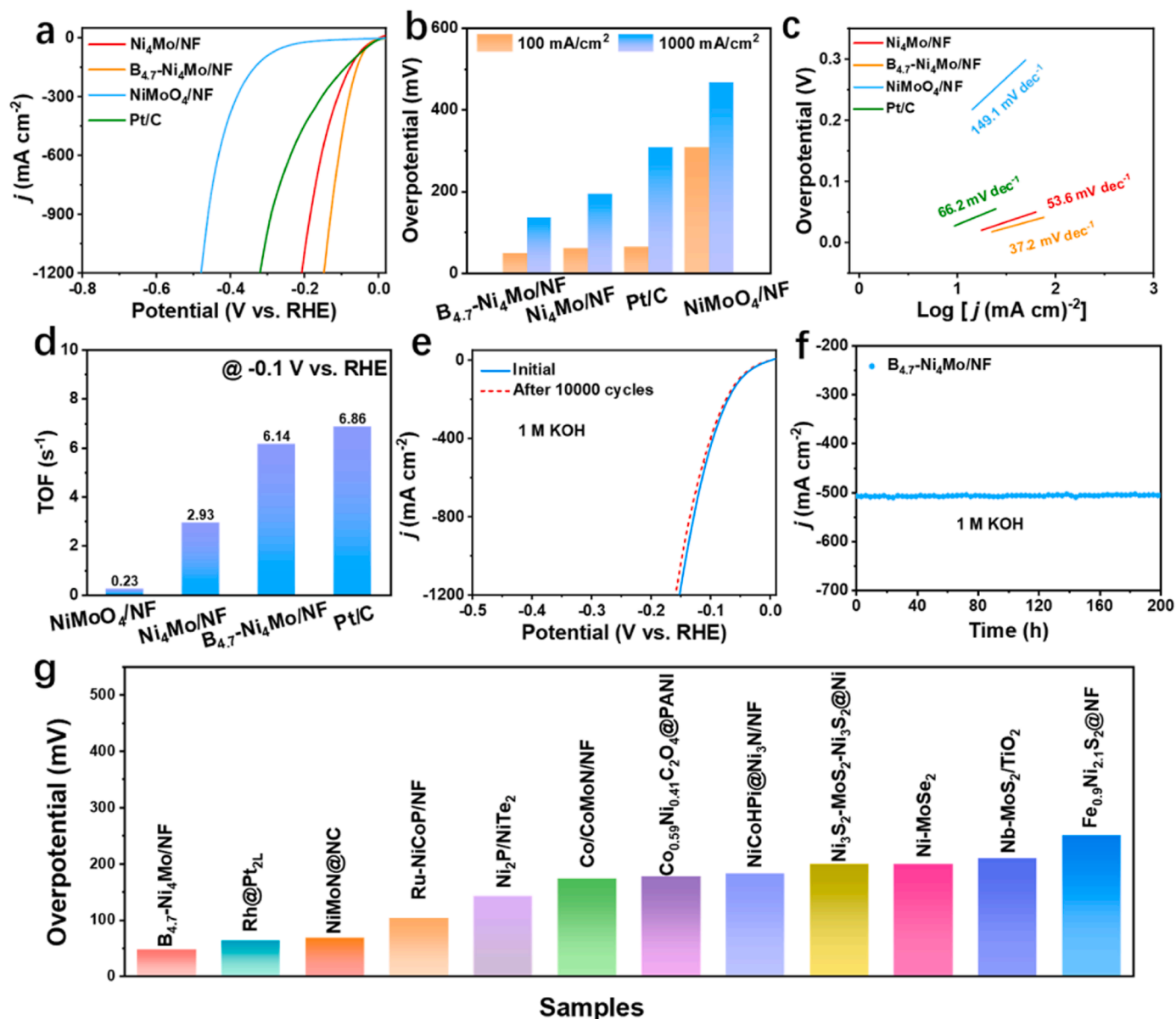


Fig. 3. The electrocatalytic HER performance of $B_{4.7}\text{-Ni}_4\text{Mo/NF}$ and contrast catalysts in 1.0 M KOH. (a) HER polarization curves; (b) overpotentials at 100 mA cm⁻² and 1000 mA cm⁻²; (c) Tafel slope plots; (d) TOF values; (e) The HER polarization curves before and after multiple cycles (f) Chronoamperometry tests under 500 mA cm⁻² in 1.0 M KOH; (g) Comparison of the overpotential at 100 mA cm⁻² for $B_{4.7}\text{-Ni}_4\text{Mo/NF}$ and recently reported HER catalysts in 1.0 M KOH.

$\text{Ni}_4\text{Mo/NF}$ (Fig. 3b). In addition, The $B_{4.7}\text{-Ni}_4\text{Mo/NF}$ exhibits an extremely low overpotential of 135.2 mV at an industrial-grade current density of 1000 mA cm⁻². Excitingly, compared with the recently reported catalysts, $B_{4.7}\text{-Ni}_4\text{Mo/NF}$ shows best catalytic activity [17,39,40] (Fig. 3g and Table S3-S4). $B_{4.7}\text{-Ni}_4\text{Mo/NF}$ even has wonderful HER activity at a current density of 3.0 A cm⁻² (Fig. S8), which has great practical application prospects. Compared with other catalysts, $B_{4.7}\text{-Ni}_4\text{Mo/NF}$ has the lowest Tafel slope of 37.2 mV dec⁻¹ (Fig. 3c), indicating that it has the optimal reaction kinetics. [41] To further investigate the origin of $B_{4.7}\text{-Ni}_4\text{Mo/NF}$'s high HER performance, we examined its electric double layer capacitance (C_{dl}) (Fig. S10), obtained from cyclic voltammetry (CV) curves with varying scan rates (Fig. S9). Using C_{dl} , we calculated the electrochemical active surface area (ECSA) of the catalyst (Fig. S11). Surprisingly, the ECSA of $B_{4.7}\text{-Ni}_4\text{Mo/NF}$ is comparable to that of $\text{Ni}_4\text{Mo/NF}$, indicating that the interstitial B atoms do not significantly contribute to improving catalytic activity by creating more active sites. [29] To further investigate the intrinsic activity of the catalysts, we analyzed the exchange current density (j_0) [42]

and turnover frequency (TOF) of the catalysts. The j_0 (Fig. S12) for $B_{4.7}\text{-Ni}_4\text{Mo/NF}$ is 8.21 mA cm⁻², which is higher than that of $\text{Ni}_4\text{Mo/NF}$ (7.42 mA cm⁻²) and Pt/C (4.43 mA cm⁻²). It exhibits excellent electron transfer rates for the $B_{4.7}\text{-Ni}_4\text{Mo/NF}$ surface. It is worth noting that the TOF (Fig. 3d and Fig. S13) of $B_{4.7}\text{-Ni}_4\text{Mo/NF}$ at 100 mV overpotential is 6.14 s⁻¹, which is almost twice as high as that of $\text{Ni}_4\text{Mo/NF}$ (2.93 s⁻¹) and even closes to that of Pt/C (6.86 s⁻¹), exhibiting excellent intrinsic activity. [43] It shows the doping of interstitial B atoms optimize the intrinsic activity of $\text{Ni}_4\text{Mo/NF}$. (Table S5). Additionally, electrochemical impedance spectroscopy (EIS) shows that $B_{4.7}\text{-Ni}_4\text{Mo/NF}$ has a lower resistance compared to $\text{Ni}_4\text{Mo/NF}$, Pt/C (Fig. S14), demonstrating that the introduction of B atoms reduces the barrier of electron transfer.

3.3. Analysis of stability

Although it is crucial to attain significant HER activity, stability is likely to be more critical in practical applications for water-splitting. [44] Therefore, we focused on evaluating the durability of

$B_{4.7}\text{-Ni}_4\text{Mo/NF}$. After 10,000 cycles of CV, it is observed that the polarization curve of $B_{4.7}\text{-Ni}_4\text{Mo/NF}$ (Fig. 3e) remains essentially unchanged compared to that of $\text{Ni}_4\text{Mo/NF}$ (Fig. S15a). Chronoamperometry (CA) analysis shows that the HER current density of $B_{4.7}\text{-Ni}_4\text{Mo/NF}$ is stable at 500 mA cm^{-2} for more than 200 h (Fig. 3f). The current density of $\text{Ni}_4\text{Mo/NF}$ decreases by nearly 100 mA cm^{-2} in just 100 h (Fig. S15b). It indicates that the introduction of B atoms improves the durability of $\text{Ni}_4\text{Mo/NF}$. To further investigate the reason for the improved stability of $B_{4.7}\text{-Ni}_4\text{Mo/NF}$, we used ICP-AES to detect the content of elemental Ni and Mo in the electrolyte. After the stability test for 48 h at a current density of 500 mA cm^{-2} , the dissolved amount of Mo and Ni account for 36.33% and 0.17% in $\text{Ni}_4\text{Mo/NF}$, respectively. However, the dissolved amount of Mo and Ni are only 3.58% and 0.15% in $B_{4.7}\text{-Ni}_4\text{Mo/NF}$ (Fig. S16 and Table S2). It confirms that the dissolution of Mo is responsible for the reduced stability of $\text{Ni}_4\text{Mo/NF}$. Interstitial B doping inhibits the dissolution of Mo in alkaline HER. The dissolution of Mo is further verified by in situ Raman spectroscopy. We first characterized the catalysts by Raman spectroscopy. The three peaks at 828, 871, and 948 cm^{-1} in $\text{NiMoO}_4\text{/NF}$ can be attributed to the Ni-O-Mo stretching vibrations, while the peak at 353 cm^{-1} is assignable to Mo-O vibrations.[15,23,45] $B_{4.7}\text{-Ni}_4\text{Mo/NF}$ displayed no Raman peaks, while Ni_4Mo exhibited a small peak at 948 cm^{-1} , possibly due to slight oxidation of Ni_4Mo . (Fig. S17). We conducted in situ Raman characterization of the catalysts once more. The initial $\text{Ni}_4\text{Mo/NF}$ and $B_{4.7}\text{-Ni}_4\text{Mo/NF}$ displayed no response signal. However, in $\text{Ni}_4\text{Mo/NF}$, a peak at 894 cm^{-1} , centered at -0.03 V vs. reversible hydrogen electrode (RHE), was observed. This peak can be attributed to the symmetric stretching vibration of Mo=O in the MoO_4 tetrahedra.[19], indicating that Mo is dissolved by the alkaline solution and transformed to MoO_4^{2-} . At -0.13 V vs. reversible hydrogen electrode (RHE), a signal peak is observed at 318 cm^{-1} , which could also be assigned to the Mo=O vibration, and the signal peak at 894 cm^{-1} is significantly enhanced (Fig. 4a). And the signal peak belonging to Mo=O also appears in $B_{4.7}\text{-Ni}_4\text{Mo/NF}$, but the peak intensity is much lower than that of $\text{Ni}_4\text{Mo/NF}$ (Fig. 4b), which also further proves that the introduction of B stabilizes the metal Mo, especially at high current density. No Raman peaks associated with Ni-O vibrations were detected in either of the catalysts, indicating the stability of Ni. According to reports[19], the solubility of Mo in alkaline HER is due to the very negative oxidation potential of Mo to MoO_4^{2-} . Interstitial B doping inhibits the formation of MoO_4^{2-} in alkaline HER. In addition, the $B_{4.7}\text{-Ni}_4\text{Mo/NF}$ after HER stability test is characterized by SEM, XRD and XPS (Fig. S18 and S19). The morphology of the reaction is basically unchanged. The XRD characteristic peaks are basically the same as before the reaction, but the intensity is weakened. The boron-metal bond still exists in XPS, indicating that the interstitial B atoms are not leached, which can continuously and effectively inhibit the dissolution of Mo and improve the durability of

$\text{Ni}_4\text{Mo/NF}$.

3.4. Theoretical calculations

We investigated the operating mechanism of Ni and Mo atoms in alkaline hydrogen evolution reaction (HER) through experiments and density functional theory (DFT) calculations, and assessed the impact of interstitial B atoms on improving the activity and stability of $\text{Ni}_4\text{Mo/NF}$. Based on catalyst performance, we conclude that the catalyst mainly undergoes the Volmer step to activate water adsorption and the Heyrovsky step for H_2 release through binding with H^* . [1,46] The water adsorption energies of Ni and Mo sites were calculated for Ni_4Mo and $B_{4.7}\text{-Ni}_4\text{Mo/NF}$, respectively (Fig. 5b). The adsorption energy of Ni site in $B_{4.7}\text{-Ni}_4\text{Mo/NF}$ and $\text{Ni}_4\text{Mo/NF}$ is greater than that of Mo site, indicating that water molecules preferentially adsorb to the Ni site. The water adsorption energy of the Mo site in $\text{Ni}_4\text{Mo/NF}$ became weaker after the introduction of the interstitial B atom, which also indicates that the introduction of B weakens the oxytrophism of Mo. We calculated the activation energies for the dissociation of H_2O^* to H^* and OH^* on the surfaces of $\text{Ni}_4\text{Mo/NF}$ and $B_{4.7}\text{-Ni}_4\text{Mo/NF}$ (Fig. 5c). The findings indicate that the activation energy of H_2O in $B_{4.7}\text{-Ni}_4\text{Mo/NF}$ is significantly lower than that in $\text{Ni}_4\text{Mo/NF}$, particularly at the Ni site. The electronic structure of $\text{Ni}_4\text{Mo/NF}$ is influenced by the interstitial B atom, resulting in a reduction of the water dissociation energy barrier and improved reaction kinetics. The H-O-H bending vibration peaks on $B_{4.7}\text{-Ni}_4\text{Mo/NF}$ (1635.94 cm^{-1}) have shifted to lower wavenumbers compared to Ni_4Mo (1636.88 cm^{-1}), demonstrating that the presence of B atoms promotes water decomposition (Fig. S20a). As hydrolysis progresses, the peak gradually shifts from 1635.94 cm^{-1} to 1634.64 cm^{-1} , indicating a gradual weakening of the O-H bond [47] (Fig. S20b). We then calculated the Gibbs free energy of adsorption of H^* on the catalyst surface (ΔGH^*) (Fig. 5d). The Mo site of $B_{4.7}\text{-Ni}_4\text{Mo/NF}$ exhibited optimal H^* adsorption with a ΔGH^* value of -0.16 eV , which was significantly lower than that of $\text{Ni}_4\text{Mo/NF}$ ($\Delta\text{GH}^* = -0.39\text{ eV}$). These results suggest that the introduction of B enhances the Heyrovsky step.[16,48,49] We have derived the reaction mechanism of $B_{4.7}\text{-Ni}_4\text{Mo/NF}$ (Fig. 5a): during the reaction, H_2O adsorbs onto the Ni site and undergoes hydrolysis, with the resulting H^* adsorbing to the Mo site for desorption. This leads to a more effective use of the Ni and Mo active sites, resulting in improved HER efficiency. The interstitial B atom itself does not serve as an active site, but instead enhances the intrinsic activity of the catalyst by modifying the electronic structure of $\text{Ni}_4\text{Mo/NF}$. Further details of the HER mechanism derivation model can be found in the supporting information. (Fig. S21-25). To further clarify the role of interstitial boron atoms, we analyzed the total density of states (DOS) and projected density of states (PDOS). Following Sabatier's principle, it is evident that Ni and Mo overly adsorb to H^* , as they are positioned to the left of the volcano

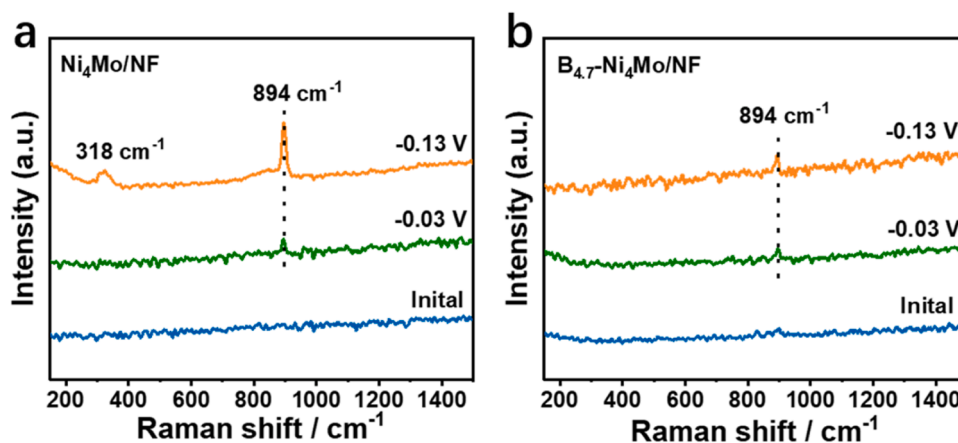


Fig. 4. Potential-dependent in-situ Raman spectra of (a) $\text{Ni}_4\text{Mo/NF}$ and (b) $B_{4.7}\text{-Ni}_4\text{Mo/NF}$.

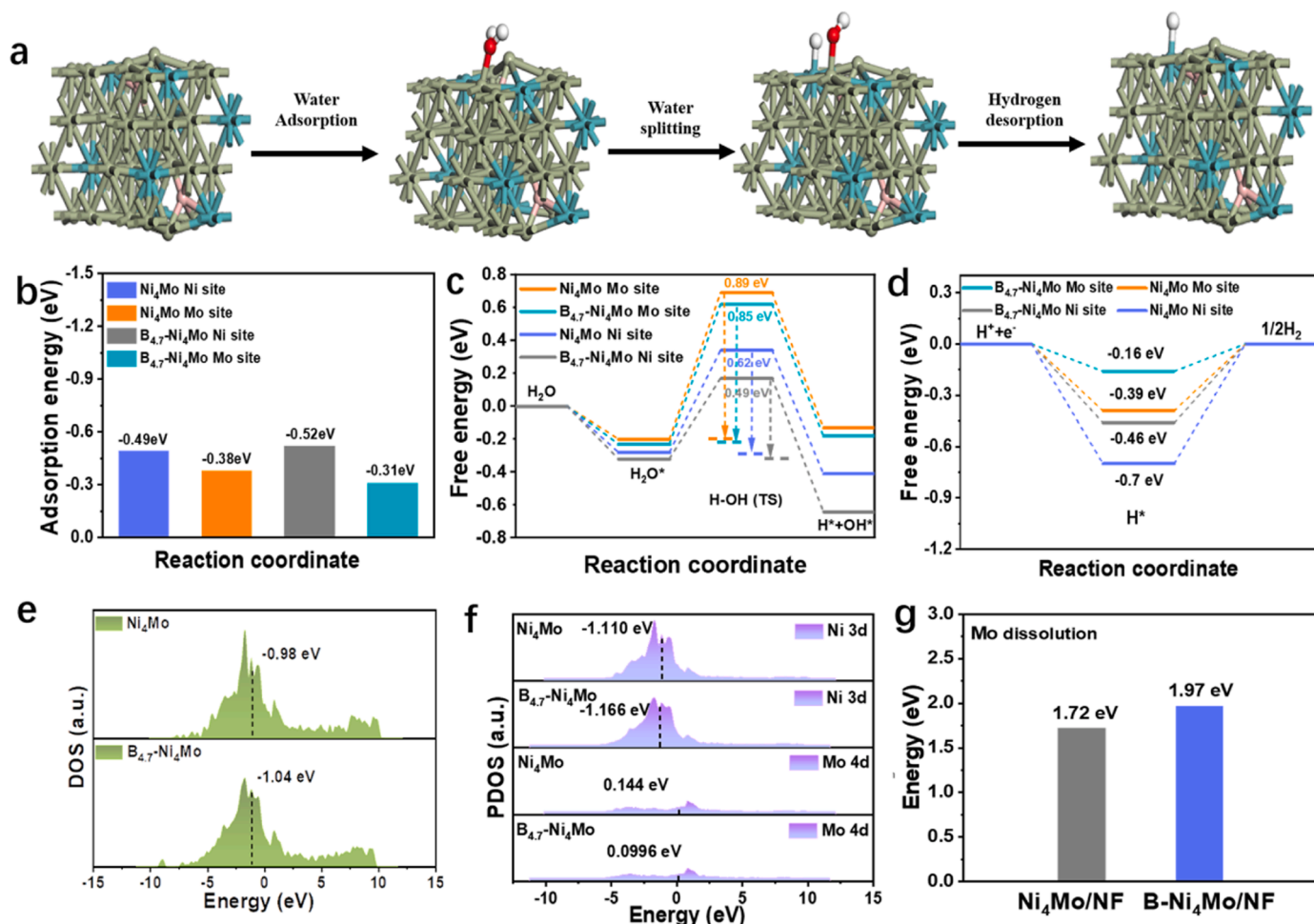


Fig. 5. (a) Schematic illustration of the proposed reaction mechanism on $B_{4.7}-Ni_4Mo/NF$ (Light green, blue, pink, red and white spheres representing Ni, Mo, B, O and H atoms); (b) Adsorption free energy of H_2O ; (c) Free energy diagram for H_2O activation (cleavage of O-H bonds of H_2O molecules); (d) Free energy diagram for H adsorption on the (121) surface of Ni_4Mo/NF and $B_{4.7}-Ni_4Mo/NF$; (e) Total DOS of Ni_4Mo/NF and $B_{4.7}-Ni_4Mo/NF$; (f) Calculated PDOS of different catalysts with d-band center positions; (g) Calculated energies for Mo dissolution of Ni_4Mo/NF and $B_{4.7}-Ni_4Mo/NF$.

top. The total DOS (Fig. 5e) reveals that the introduction of boron atoms shifts the d-band center of Ni_4Mo/NF away from the Fermi energy level, indicating that it weakens the H^* adsorption.[50] The PDOS analysis (Fig. 5f) indicates that the d-band centers of the Ni and Mo active sites in $B_{4.7}-Ni_4Mo/NF$ are negatively shifted in comparison to those in Ni_4Mo/NF . This can be attributed to the hybridization of the 3d orbital of Ni and the 4d orbital of Mo with the p orbital of boron, resulting in the occupation of the empty orbital of boron by the electrons from Ni and Mo. Subsequently, the charge density of these metal sites is reduced. These findings reveal that interstitial boron doping not only enhances the aqueous dissociation capacity of Ni_4Mo/NF , but also regulates the adsorption of H^* on Ni_4Mo/NF to improve the HER performance of the catalyst.

To further evaluate the role of the interstitial B atom in enhancing the stability of Ni_4Mo/NF [51], we calculated the enthalpy change of the dissolution process of Mo atoms of Ni_4Mo/NF and $B_{4.7}-Ni_4Mo/NF$, and showed the free energy change of the dissolution process of Mo (Fig. S26-S27, Table S5 and Supplementary Note). We find that introducing interstitial B atoms into the lattice of Ni_4Mo/NF increases the energy of Mo detachment from 1.72 eV to 1.97 eV (Fig. 5g), indicating greater stability of Mo in $B_{4.7}-Ni_4Mo/NF$ compared to Ni_4Mo/NF . DFT simulations also reveal that the enthalpy lost by the interstitial B atom is 1.45 V (Fig. S28), rendering detachment more difficult and stabilizing the $B_{4.7}-Ni_4Mo/NF$ structure. These results demonstrate that interstitial B atoms strongly interact with Mo, inhibiting its dissolution in alkali

solutions. Furthermore, B is stably present in Ni_4Mo interstitials, enhancing the stability of Ni_4Mo/NF .

3.5. AEM device performance

Based on the outstanding stability and activity demonstrated by the $B_{4.7}-Ni_4Mo/NF$ catalyst in a three-electrode system, we conducted further assessments of its suitability for practical applications in water electrolysis.[5] We constructed an AEM electrolytic cell with $B_{4.7}-Ni_4Mo/NF$ as cathode and IrO_2 on nickel foam as anode, and tested its performance at 60 °C (Fig. 6a and Fig. S29). IrO_2 was chosen because of its excellent durability and activity in OER. The polarization curve shows that $B_{4.7}-Ni_4Mo/NF || IrO_2/NF$ has better water electrolytic activity than $Ni_4Mo/NF || IrO_2/NF$ electrolytic cell. Specifically, at 1.0 M KOH, the cell based on $B_{4.7}-Ni_4Mo/NF$ requires only 1.73 V to reach a current density of 1.0 A cm⁻² (Fig. 6b), which shows excellent catalytic properties. Furthermore, we conducted gas chromatography analysis (Fig. 6c) on the gas products and evaluated the Faraday efficiency in 1.0 M KOH. Our results showed that the hydrogen production had a Faraday efficiency close to 100%, indicating a remarkably high electron utilization rate in the HER process. Additionally, we carried out chrono-potential tests on $B_{4.7}-Ni_4Mo/NF || IrO_2/NF$ to assess the long-term stability of AEM electrolysis. The $B_{4.7}-Ni_4Mo/NF || IrO_2/NF$ electrolyzer was operated continuously for 800 h at a current density of 1.0 A cm⁻² with negligible changes in the electrolyzer voltage (Fig. 6d).

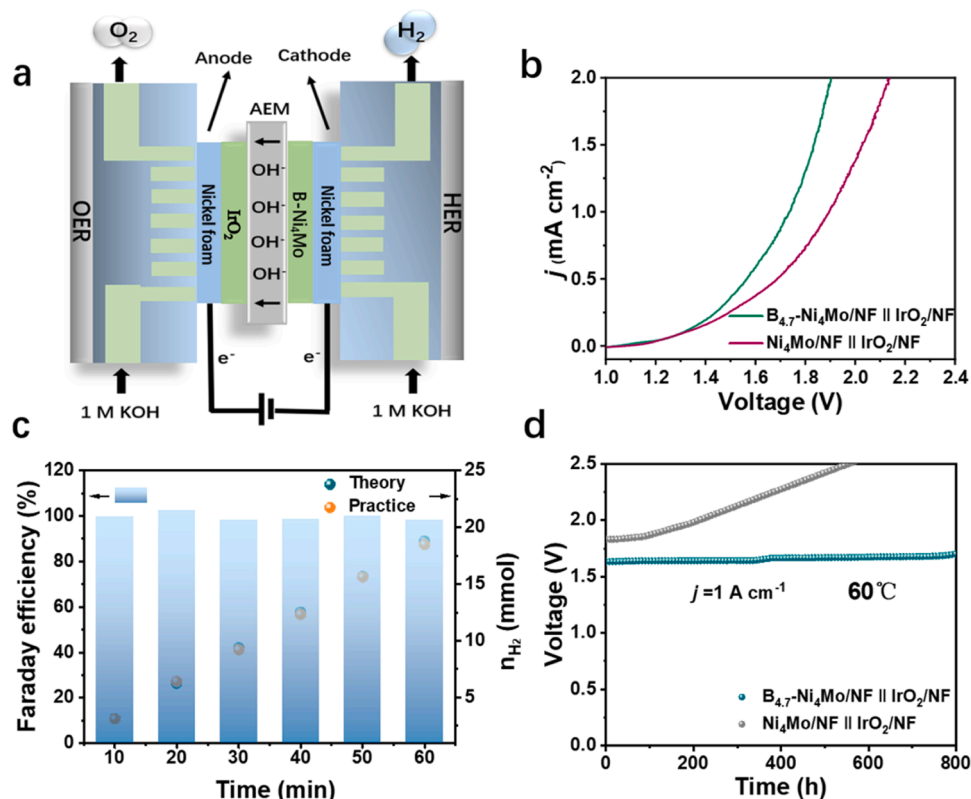


Fig. 6. The performance of the $B_{4.7}\text{-Ni}_4\text{Mo/NF}$ catalyst for the AEM electrolyser at 60 °C (a) Schematic diagram of an AEM electrolyser. (b) Polarization curve of the $B_{4.7}\text{-Ni}_4\text{Mo/NF} \parallel \text{IrO}_2\text{/NF}$ couple in an AEM electrolyser. (c) Faradaic efficiency, and theoretical and experimental results of H_2 production of $B_{4.7}\text{-Ni}_4\text{Mo/NF}$. (d) Chronopotentiometry curve for AEM electrolysis using $B_{4.7}\text{-Ni}_4\text{Mo/NF}$ and $\text{IrO}_2\text{/NF}$ as cathode and anode catalysts operating at 1.0 A cm^{-2} .

After 200 h of electrolysis in $\text{Ni}_4\text{Mo/NF} \parallel \text{IrO}_2\text{/NF}$ electrolyzer under the same test conditions, the electrolyzer voltage is found to be significantly higher. These stability test results show that the introduction of interstitial B atoms enhances the stability of $\text{Ni}_4\text{Mo/NF}$. And the $B_{4.7}\text{-Ni}_4\text{Mo/NF}$ catalyst has promising applications in AEM electrolytic water.

4. Conclusion

In summary, interstitial boron atom-doped Ni_4Mo on NF is designed to obtain the catalyst with excellent alkaline HER properties. In 1.0 M KOH, the overpotential of $B_{4.7}\text{-Ni}_4\text{Mo/NF}$ at 100 mA cm^{-2} is 47.4 mV. Especially at the high current density of 1000 mA cm^{-2} , the overpotential is only 135.2 mV. More specifically, the turnover frequency calculation (TOF) of $B_{4.7}\text{-Ni}_4\text{Mo/NF}$ is about 6.14 s^{-1} (-0.1 V vs. RHE), which is four times higher than that of $\text{Ni}_4\text{Mo/NF}$ (1.34 s^{-1}) and is very close to that of Pt/C (6.86 s^{-1}). Moreover, $B_{4.7}\text{-Ni}_4\text{Mo/NF}$ not only exhibits stability for over 200 h at the high current density of 500 mA cm^{-2} but also stably operates at 1.0 A cm^{-2} over 800 h at 60 °C AEM electrolyser. Through experimental and theoretical calculations, we have verified that in $B_{4.7}\text{-Ni}_4\text{Mo/NF}$, Ni acts as the site of water adsorption and desorption, and the generated H^* is adsorbed and desorbed at the Mo site. The excellent HER properties are attributed to doping of interstitial boron atoms, which not only optimizes the electronic structure with a descending d-band center to weaken H^* adsorption but also reduces the water dissociation energy barrier. The strong interaction of boron-metal bond weakens the adsorption of OH^- by reducing the oxytropy of Mo, thus inhibiting the dissolution of Mo in alkaline HER. Our work firstly provides a simple interstitial doping strategy which can optimize the adsorption of different intermediates while improving stability. This strategy provides a new way to design industrial electrocatalytic systems.

CRediT authorship contribution statement

Lei Wang and Jianping Lai supervised the research. Jianping Lai conceived the research. Jianping Lai and Pengfei Liu designed the experiments. Pengfei Liu performed most of the experiments and data analysis. Yue Shi helped analyze physical characterization data and helped supplement experimental data. Xin Zhang prepared the electrodes and helped with electrochemical measurements. Jiao Yin and Dan Zhang helped analyze physical characterization data. Tiantian Wang, Jiawei Fei and Tianrong Zhan helped answer some questions. Guangjiu Li provided some of the data support and explanations for the questions. All authors discussed the results and commented on the manuscript.

Declaration of Competing Interest

The authors declare that they have no known competing financial interests or personal relationships that could have appeared to influence the work reported in this paper.

Data availability

The authors do not have permission to share data.

Acknowledgments

This work was supported by the National Natural Science Foundation of China (51772162, 22001143, and 52072197), Youth Innovation and Technology Foundation of Shandong Higher Education Institutions, China (2019KJC004), Outstanding Youth Foundation of Shandong Province, China (ZR2019JQ14), Taishan Scholar Young Talent Program (tsqn201909114, tsqn201909123), Natural Science Foundation of

Shandong Province (ZR2020YQ34), Major Scientific and Technological Innovation Project (2019JZZY020405), and Major Basic Research Program of Natural Science Foundation of Shandong Province under Grant (ZR2020ZD09).

Appendix A. Supporting information

Supplementary data associated with this article can be found in the online version at [doi:10.1016/j.apcatb.2023.123332](https://doi.org/10.1016/j.apcatb.2023.123332).

References

- X. Wang, G. Long, B. Liu, Z. Li, W. Gao, P. Zhang, H. Zhang, X. Zhou, R. Duan, W. Hu, C. Li, Rationally modulating the functions of $\text{Ni}_3\text{Sn}_2\text{-NiSnO}_x$ nanocomposite electrocatalysts towards enhanced hydrogen evolution reaction, *Angew. Chem. Int. Ed.* 62 (2023) 202301562, <https://doi.org/10.1002/anie.202301562>.
- D. Zhang, H. Miao, X. Wu, Z. Wang, H. Zhao, Y. Shi, X. Chen, Z. Xiao, J. Lai, L. Wang, Scalable synthesis of ultra-small $\text{Ru}_2\text{P@Ru/CNT}$ for efficient seawater splitting, *Chin. J. Catal.* 43 (2022) 1148–1155, [https://doi.org/10.1016/S1872-2067\(21\)64012-3](https://doi.org/10.1016/S1872-2067(21)64012-3).
- K. Deng, T. Zhou, Q. Mao, S. Wang, Z. Wang, Y. Xu, X. Li, H. Wang, L. Wang, Surface engineering of defective and porous Ir metallene with polyallylamine for hydrogen evolution electrocatalysis, *Adv. Mater.* 34 (2022), 2110680, <https://doi.org/10.1002/adma.202110680>.
- X. Wu, Z. Wang, D. Zhang, Y. Qin, M. Wang, Y. Han, T. Zhan, B. Yang, S. Li, J. Lai, L. Wang, Solvent-free microwave synthesis of ultra-small $\text{Ru-mo}_2\text{c@cnt}$ with strong metal-support interaction for industrial hydrogen evolution, *Nat. Commun.* 12 (2021), 4018, <https://doi.org/10.1038/s41467-021-24322-2>.
- L. Gao, F. Bao, X. Tan, M. Li, Z. Shen, X. Chen, Z. Tang, W. Lai, Y. Lu, P. Huang, C. Ma, S.C. Smith, Z. Ye, Z. Hu, H. Huang, Engineering a local potassium cation concentrated microenvironment toward the ampere-level current density hydrogen evolution reaction, *Energy Environ. Sci.* 16 (2023) 285–294, <https://doi.org/10.1039/d2ee02836k>.
- I. Vincent, D. Bessarabov, Low cost hydrogen production by anion exchange membrane electrolysis: A review, *Renew. Sust. Energ. Rev.* 81 (2018) 1690–1704, <https://doi.org/10.1016/j.rser.2017.05.258>.
- P. Chen, X. Hu, High-efficiency anion exchange membrane water electrolysis employing non-noble metal catalysts, *Adv. Energy Mater.* 10 (2020), 2002285, <https://doi.org/10.1002/aenm.202002285>.
- X. Wang, X. Liu, S. Wu, K. Liu, X. Meng, B. Li, J. Lai, L. Wang, S. Feng, Phosphorus vacancies enriched cobalt phosphide embedded in nitrogen doped carbon matrix enabling seawater splitting at ampere-level current density, *Nano Energy* 109 (2023), 108292, <https://doi.org/10.1016/j.nanoen.2023.108292>.
- Y. Luo, Z. Zhang, F. Yang, J. Li, Z. Liu, W. Ren, S. Zhang, B. Liu, Stabilized hydroxide-mediated nickel-based electrocatalysts for high-current-density hydrogen evolution in alkaline media, *Energy Environ. Sci.* 14 (2021) 4610–4619, <https://doi.org/10.1039/d1ee01487k>.
- W. Yu, H. Huang, Y. Qin, D. Zhang, Y. Zhang, K. Liu, Y. Zhang, J. Lai, L. Wang, The synergistic effect of pyrrolic-n and pyridinic-n with Pt under strong metal-support interaction to achieve high-performance alkaline hydrogen evolution, *Adv. Energy Mater.* 12 (2022), 2200110, <https://doi.org/10.1002/aenm.202200110>.
- H. Jin, B. Ruyia, Y. Park, H.J. Kim, H.S. Oh, S.I. Choi, K. Lee, Nanocatalyst design for long-term operation of proton/anion exchange membrane water electrolysis, *Adv. Energy Mater.* 11 (2020), 2003188, <https://doi.org/10.1002/aenm.202003188>.
- J. Zhang, T. Wang, P. Liu, Z. Liao, S. Liu, X. Zhuang, M. Chen, E. Zschech, X. Feng, Efficient hydrogen production on MoNi_4 electrocatalysts with fast water dissociation kinetics, *Nat. Commun.* 8 (2017), 15437, <https://doi.org/10.1038/ncomms15437>.
- J. Hou, Y. Wu, B. Zhang, S. Cao, Z. Li, L. Sun, Rational design of nanoarray architectures for electrocatalytic water splitting, *Adv. Funct. Mater.* 29 (2019), 1808367, <https://doi.org/10.1002/adfm.201808367>.
- S.H. Park, D.T. To, N.V. Myung, A review of nickel-molybdenum based hydrogen evolution electrocatalysts from theory to experiment, *Appl. Catal. A Gen.* 651 (2023), 119013, <https://doi.org/10.1016/j.apcata.2022.119013>.
- Y. Chen, Y. Zhang, X. Zhang, T. Tang, H. Luo, S. Niu, Z. Dai, L. Wan, J. Hu, Self-templated fabrication of $\text{MoNi}_4/\text{MoO}_3\text{-x}$ nanorod arrays with dual active components for highly efficient hydrogen evolution, *Adv. Mater.* 29 (2017), 1703311, <https://doi.org/10.1002/adma.201703311>.
- L. Yu, I.K. Mishra, Y. Xie, H. Zhou, J. Sun, J. Zhou, Y. Ni, D. Luo, F. Yu, Y. Yu, S. Chen, Z. Ren, Ternary $\text{Ni}_{2(1-x)}\text{Mo}_{2x}\text{P}$ nanowire arrays toward efficient and stable hydrogen evolution electrocatalysis under large-current-density, *Nano Energy* 53 (2018) 492–500, <https://doi.org/10.1016/j.nanoen.2018.08.025>.
- L. Wu, F. Zhang, S. Song, M. Ning, Q. Zhu, J. Zhou, G. Gao, Z. Chen, Q. Zhou, X. Xing, T. Tong, Y. Yao, J. Bao, L. Yu, S. Chen, Z. Ren, Efficient alkaline water/seawater hydrogen evolution by a nanorod-nanoparticle-structured Ni-mo catalyst with fast water-dissociation kinetics, *Adv. Mater.* 34 (2022), 2201774, <https://doi.org/10.1002/adma.202201774>.
- M. Wang, H. Yang, J. Shi, Y. Chen, Y. Zhou, L. Wang, S. Di, X. Zhao, J. Zhong, T. Cheng, W. Zhou, Y. Li, Alloying nickel with molybdenum significantly accelerates alkaline hydrogen electrocatalysis, *Angew. Chem. Int. Ed.* 60 (2021) 5771–5777, <https://doi.org/10.1002/anie.202013047>.
- W. Du, Y. Shi, W. Zhou, Y. Yu, B. Zhang, Unveiling the in situ dissolution and polymerization of Mo in Ni_4Mo alloy for promoting the hydrogen evolution reaction, *Angew. Chem. Int. Ed.* 60 (2021) 7051–7055, <https://doi.org/10.1002/anie.202015723>.
- Y. Ito, T. Ohto, D. Hojo, M. Wakasaka, Y. Nagata, L. Chen, K. Hu, M. Izumi, J.-i. Fujita, T. Adschiri, Cooperation between holey graphene and NiMo alloy for hydrogen evolution in an acidic electrolyte, *ACS Catal.* 8 (2018) 3579–3586, <https://doi.org/10.1021/acscatal.7b04091>.
- X. Bu, X. Liang, Y. Bu, Q. Quan, Y. Meng, Z. Lai, W. Wang, C. Liu, J. Lu, C.-M. Lawrence Wu, J.C. Ho, NiMo@ C_3N_5 heterostructures with multiple electronic transmission channels for highly efficient hydrogen evolution from alkaline electrolytes and seawater, *Chem. Eng. J.* 438 (2022), 135379, <https://doi.org/10.1016/j.cej.2022.135379>.
- L. Peng, J. Min, A. Bendavid, D. Chu, X. Lu, R. Amal, Z. Han, Stabilizing the unstable: Chromium coating on NiMo electrode for enhanced stability in intermittent water electrolysis, *ACS Appl. Mater. Interfaces* 14 (2022) 40822–40833, <https://doi.org/10.1021/acsaami.2c09004>.
- J.H.J. Wijten, R.L. Riemersma, J. Gauthier, L.D.B. Mandemaker, M. Verhoeven, J. P. Hofmann, K. Chan, B.M. Weckhuysen, Electrolyte effects on the stability of Ni-Mo cathodes for the hydrogen evolution reaction, *ChemSusChem* 12 (2019) 3491–3500, <https://doi.org/10.1002/cssc.201900617>.
- T. Wang, M. Wang, H. Yang, M. Xu, C. Zuo, K. Feng, M. Xie, J. Deng, J. Zhong, W. Zhou, T. Cheng, Y. Li, Weakening hydrogen adsorption on nickel via interstitial nitrogen doping promotes bifunctional hydrogen electrocatalysis in alkaline solution, *Energy Environ. Sci.* 12 (2019) 3522–3529, <https://doi.org/10.1039/c9ee01743g>.
- Y. Niu, X. Huang, Y. Wang, M. Xu, J. Chen, S. Xu, M.-G. Willinger, W. Zhang, M. Wei, B. Zhang, $(\text{Ni}_3\text{ZnCo}_7/\text{OCNT})$ manipulating interstitial carbon atoms in the nickel octahedral site for highly efficient hydrogenation of alkyne, *Nat. Commun.* 11 (2020), 3324, <https://doi.org/10.1038/s41467-020-17188-3>.
- L. Wang, Z. Zeng, W. Gao, T. Maxson, D. Raciti, M. Giroux, X. Pan, C. Wang, J. Greeley, Tunable intrinsic strain in two-dimensional transition metal electrocatalysts, *Science* 363 (2019) 870–874, <https://doi.org/10.1126/science.aat8051>.
- J. Cai, Y. Song, Y. Zang, S. Niu, Y. Wu, Y. Xie, X. Zheng, Y. Liu, Y. Lin, X. Liu, G. Wang, Y. Qian, N-induced lattice contraction generally boosts the hydrogen evolution catalysis of p-rich metal phosphides, *Sci. Adv.* 6 (2020), eaaw8113, <https://doi.org/10.1126/sciadv.aaw8113>.
- J. Zhao, B. Chen, F. Wang, Shedding light on the role of misfit strain in controlling core-shell nanocrystals, *Adv. Mater.* 32 (2020), 2004142, <https://doi.org/10.1002/adma.202004142>.
- J. Liu, Z. Wang, X. Wu, D. Zhang, Y. Zhang, J. Xiong, Z. Wu, J. Lai, L. Wang, Pt doping and strong metal-support interaction as a strategy for NiMo-based electrocatalysts to boost the hydrogen evolution reaction in alkaline solution, *J. Mater. Chem. A* 10 (2022) 15395–15401, <https://doi.org/10.1039/d2ta03934f>.
- G. Liu, H. Bai, Y. Ji, L. Wang, Y. Wen, H. Lin, L. Zheng, Y. Li, B. Zhang, H. Peng, A highly efficient alkaline HER Co-Mo bimetallic carbide catalyst with an optimized Mo d-orbital electronic state, *J. Mater. Chem. A* 7 (2019) 12434–12439, <https://doi.org/10.1039/c9ta02886b>.
- X. Ai, X. Zou, H. Chen, Y. Su, X. Feng, Q. Li, Y. Liu, Y. Zhang, X. Zou, Transition-metal-boron intermetallics with strong interatomic d-sp orbital hybridization for high-performance electrocatalysis, *Angew. Chem. Int. Ed.* 59 (2020) 3961–3965, <https://doi.org/10.1002/anie.201915663>.
- Y. Gao, S. Qian, H. Wang, W. Yuan, Y. Fan, N. Cheng, H. Xue, T. Jiang, J. Tian, Boron-doping on the surface mediated low-valence Co centers in cobalt phosphide for improved electrocatalytic hydrogen evolution, *Appl. Catal. B Environ.* 320 (2023), 122014, <https://doi.org/10.1016/j.apcatb.2022.122014>.
- C. Zhang, W. Liu, C. Chen, P. Ni, B. Wang, Y. Jiang, Y. Lu, Emerging interstitial/substitutional modification of Pd-based nanomaterials with nonmetallic elements for electrocatalytic applications, *Nanoscale* 14 (2022) 2915–2942, <https://doi.org/10.1039/d1nr06570j>.
- I.S. Kwon, I.H. Kwak, S.Y. Ju, S. Kang, S. Han, Y.C. Park, J. Park, J. Park, Adamant doping of transition metals in ReSe_2 nanosheets for enhanced electrocatalytic hydrogen evolution reaction, *ACS Nano* 14 (2020) 12184–12194, <https://doi.org/10.1021/acsnano.0c05874>.
- B. Ding, Y.-T. Liu, L. Tang, J. Dai, J. Yu, Promoted electrocatalytic nitrogen fixation in Fe-Ni layered double hydroxide arrays coupled to carbon nanofibers: The role of phosphorus doping, *Angew. Chem. Int. Ed.* 59 (2020) 13623–13627, <https://doi.org/10.1002/anie.202005579>.
- Q. Zhou, Z. Shen, C. Zhu, L. Jiachen, D. Zhiyuan, W. Peng, P. Feng, Z. Zhiyong, M. Haixia, W. Shuangyin, Z. Huiqiang, Nitrogen-doped cop electrocatalysts for coupled hydrogen evolution and sulfur generation with low energy consumption, *Adv. Mater.* 30 (2018), 1800140, <https://doi.org/10.1002/adma.201800140>.
- Z. Wang, M. Li, P. Wang, K. Deng, H. Yu, X. Wang, Y. Xu, H. Wang, L. Wang, Interstitial boron-doped nanoporous palladium film for electro-reduction of nitrogen to ammonia, *Chem. Eng. J.* 449 (2022), <https://doi.org/10.1016/j.cej.2022.137771>.
- X. Wang, G. Tai, Z. Wu, T. Hu, R. Wang, Ultrathin molybdenum boride films for highly efficient catalysis of the hydrogen evolution reaction, *J. Mater. Chem. A* 5 (2017) 23471–23475, <https://doi.org/10.1039/c7ta08597d>.
- H. Ma, Z. Chen, Z. Wang, C.V. Singh, Q. Jiang, Interface engineering of Co/comon/nf heterostructures for high-performance electrochemical overall water splitting, *Adv. Sci.* 9 (2022), 2105313, <https://doi.org/10.1002/adv.202105313>.
- T. Ling, T. Zhang, B. Ge, L. Han, L. Zheng, F. Lin, Z. Xu, W.-B. Hu, X.-W. Du, K. Davey, S.-Z. Qiao, Well-dispersed nickel- and zinc-tailored electronic structure

- of a transition metal oxide for highly active alkaline hydrogen evolution reaction, *Adv. Mater.* 31 (2019), 1807771, <https://doi.org/10.1002/adma.201807771>.
- [41] D. Zhang, Z. Wang, X. Wu, Y. Shi, N. Nie, H. Zhao, H. Miao, X. Chen, S. Li, J. Lai, L. Wang, Noble metal (Pt, Rh, Pd, Ir) doped Ru/CNT ultra-small alloy for acidic hydrogen evolution at high current density, *Small* 18 (2022), 2104559, <https://doi.org/10.1002/sml.202104559>.
- [42] M.A.R. Anjum, H.Y. Jeong, M.H. Lee, H.S. Shin, J.S. Lee, Efficient hydrogen evolution reaction catalysis in alkaline media by all in one MoS₂ with multifunctional active sites, *Adv. Mater.* 30 (2018), 1707105, <https://doi.org/10.1002/adma.201707105>.
- [43] P. Zhai, M. Xia, Y. Wu, G. Zhang, J. Gao, B. Zhang, S. Cao, Y. Zhang, Z. Li, Z. Fan, C. Wang, X. Zhang, J.T. Miller, L. Sun, J. Hou, Engineering single-atomic ruthenium catalytic sites on defective nickel-iron layered double hydroxide for overall water splitting, *Nat. Commun.* 12 (2021), 4587, <https://doi.org/10.1038/s41467-021-24828-9>.
- [44] L. Wan, Z. Xu, Q. Xu, P. Wang, B. Wang, Overall design of novel 3d-ordered mea with drastically enhanced mass transport for alkaline electrolyzers, *Energy Environ. Sci.* 15 (2022) 1882–1892, <https://doi.org/10.1039/d2ee00273f>.
- [45] L. Guo, J. Chi, J. Zhu, T. Cui, J. Lai, L. Wang, Dual-doping nimo₄ with multi-channel structure enable urea-assisted energy-saving H₂ production at large current density in alkaline seawater, *Appl. Catal. B Environ.* 320 (2023), 121977, <https://doi.org/10.1016/j.apcatb.2022.121977>.
- [46] Y. Li, X. Tan, R.K. Hocking, X. Bo, H. Ren, B. Johannessen, S.C. Smith, C. Zhao, Implanting Ni-o-vox sites into Cu-doped Ni for low-overpotential alkaline hydrogen evolution, *Nat. Commun.* 11 (2020), 2720, <https://doi.org/10.1038/s41467-020-16554-5>.
- [47] N. Nie, D. Zhang, Z. Wang, W. Yu, S. Ge, J. Xiong, Y. Gu, B. Yang, J. Lai, L. Wang, Stable PtNb-Nb₂O₅ heterostructure clusters @CC for high-current-density neutral seawater hydrogen evolution, *Appl. Catal. B Environ.* 318 (2022), 121808, <https://doi.org/10.1016/j.apcatb.2022.121808>.
- [48] X. Zhao, G. Wu, X. Zheng, P. Jiang, J.D. Yi, H. Zhou, X. Gao, Z.Q. Yu, Y. Wu, A double atomic-tuned RuBi SAA/Bi@OG nanostructure with optimum charge redistribution for efficient hydrogen evolution, *Angew. Chem. Int. Ed.* 62 (2023) 202300879, <https://doi.org/10.1002/anie.202300879>.
- [49] Y. Peng, C. Shan, H. Wang, L. Hong, S. Yao, R. Wu, Z. Zhang, T. Lu, Polyoxometalate-derived ultrasmall Pt₂W/WO₃ heterostructure outperforms platinum for large-current-density H₂ evolution, *Adv. Energy Mater.* 9 (2019), 1900597, <https://doi.org/10.1002/aenm.201900597>.
- [50] C. Li, S.H. Kim, H.Y. Lim, Q. Sun, Y. Jiang, H.J. Noh, S.J. Kim, J. Baek, S.K. Kwak, J.B. Baek, Self-accommodation induced electronic metal-support interaction on ruthenium site for alkaline hydrogen evolution reaction, *Adv. Mater.* 35 (2023), 2301369, <https://doi.org/10.1002/adma.202301369>.
- [51] Z. Wu, F. Chen, B. Li, S. Yu, Y. Finck, D. Meira, Q. Yan, P. Zhu, M. Chen, T. Song, Z. Yin, H. Liang, S. Zhang, G. Wang, H. Wang, Non-iridium-based electrocatalyst for durable acidic oxygen evolution reaction in proton exchange membrane water electrolysis, *Nat. Mater.* 22 (2023) 100–108, <https://doi.org/10.1038/s41563-022-01380-5>.